

***In vivo* wide-field reflectance/fluorescence imaging and polarization-sensitive optical coherence tomography of human oral cavity with a forward-viewing probe**

Yeoreum Yoon,¹ Won Hyuk Jang,² Peng Xiao,¹ Bumju Kim,¹ Taejun Wang,²
Qingyun Li,¹ Ji Youl Lee,³ Euiheon Chung,⁴ and Ki Hean Kim^{1,2,*}

¹Department of Mechanical Engineering, Pohang University of Science and Technology, San 31, Hyoja-dong, Nam-gu, Pohang, Gyeongbuk 790-784, South Korea

²Division of Integrative Biosciences and Biotechnology, Pohang University of Science and Technology, San 31, Hyoja-dong, Nam-gu, Pohang, Gyeongbuk 790-784, South Korea

³Department of Urology, College of Medicine, The Catholic University of Korea, 505 Banpo-dong, Seocho-gu, Seoul 137-040, South Korea

⁴Department of Medical System Engineering and School of Mechatronics, Gwangju Institute of Science and Technology, 123 Cheomdan-gwagiro, Buk-gu, Gwangju 500-712, South Korea
[*kiheankim@postech.edu](mailto:kiheankim@postech.edu)

Abstract: We report multimodal imaging of human oral cavity *in vivo* based on simultaneous wide-field reflectance/fluorescence imaging and polarization-sensitive optical coherence tomography (PS-OCT) with a forward-viewing imaging probe. Wide-field reflectance/fluorescence imaging and PS-OCT were to provide both morphological and fluorescence information on the surface, and structural and birefringent information below the surface respectively. The forward-viewing probe was designed to access the oral cavity through the mouth with dimensions of approximately 10 mm in diameter and 180 mm in length. The probe had field of view (FOV) of approximately 5.5 mm in diameter, and adjustable depth of field (DOF) from 2 mm to 10 mm by controlling numerical aperture (NA) in the detection path. This adjustable DOF was to accommodate both requirements for image-based guiding with high DOF and high-resolution, high-sensitivity imaging with low DOF. This multimodal imaging system was characterized by using a tissue phantom and a mouse model *in vivo*, and was applied to human oral cavity. Information of surface morphology and vasculature, and under-surface layered structure and birefringence of the oral cavity tissues was obtained. These results showed feasibility of this multimodal imaging system as a tool for studying oral cavity lesions in clinical applications.

©2015 Optical Society of America

OCIS codes: (170.4500) Optical coherence tomography; (300.2530) Fluorescence, laser-induced; (170.3880) Medical and biological imaging; (170.3890) Medical optics instrumentation.

References and links

1. American Cancer Society. Cancer Facts & Figs. 2014.
2. M. Lam, A. J. Chaudhari, Y. Sun, F. Zhou, A. Dobbie, R. F. Gandour-Edwards, S. P. Tinling, D. G. Farwell, W. L. Monsky, K. K. Shung, and L. Marcu, "Ultrasound Backscatter Microscopy for Imaging of Oral Carcinoma," *J. Ultrasound Med.* **32**(10), 1789–1797 (2013).
3. T. W. Remmerbach, H. Weidenbach, N. Pomjanski, K. Knops, S. Mathes, A. Hemprich, and A. Böcking, "Cytologic and DNA-cytometric early diagnosis of oral cancer," *Anal. Cell. Pathol.* **22**(4), 211–221 (2001).
4. C. Scully, J. V. Bagan, C. Hopper, and J. B. Epstein, "Oral cancer: current and future diagnostic techniques," *Am. J. Dent.* **21**(4), 199–209 (2008).

5. A. Zupi, L. Califano, P. Maremonti, F. Longo, R. Ciccarelli, and A. Soricelli, "Accuracy in the diagnosis of mandibular involvement by oral cancer," *J. Craniomaxillofac. Surg.* **24**(5), 281–284 (1996).
6. M. Olivo, R. Bhuvaneswari, and I. Keogh, "Advances in bio-optical imaging for the diagnosis of early oral cancer," *Pharmaceutics* **3**(4), 354–378 (2011).
7. N. Bedard, R. A. Schwarz, A. Hu, V. Bhattar, J. Howe, M. D. Williams, A. M. Gillenwater, R. Richards-Kortum, and T. S. Tkaczyk, "Multimodal snapshot spectral imaging for oral cancer diagnostics: a pilot study," *Biomed. Opt. Express* **4**(6), 938–949 (2013).
8. D. V. Messadi, F. S. Younai, H.-H. Liu, G. Guo, and C.-Y. Wang, "The clinical effectiveness of reflectance optical spectroscopy for the in vivo diagnosis of oral lesions," *Int. J. Oral Sci.* (2014).
9. D. C. G. De Veld, M. J. H. Witjes, H. J. C. M. Sterenborg, and J. L. N. Roodenburg, "The status of in vivo autofluorescence spectroscopy and imaging for oral oncology," *Oral Oncol.* **41**(2), 117–131 (2005).
10. C. Paderni, D. Compilato, F. Carinci, G. Nardi, V. Rodolico, L. Lo Muzio, G. Spinelli, M. Mazzotta, and G. Campisi, "Direct visualization of oral-cavity tissue fluorescence as novel aid for early oral cancer diagnosis and potentially malignant disorders monitoring," *Int. J. Immunopathol. Pharmacol.* **24**(2 Suppl), 121–128 (2011).
11. J. A. Jo, B. E. Applegate, J. Park, S. Shrestha, P. Pande, I. B. Gimenez-Conti, and J. L. Brandon, "In Vivo Simultaneous Morphological and Biochemical Optical Imaging of Oral Epithelial Cancer," *IEEE Trans. Biomed. Eng.* **57**(10), 2596–2599 (2010).
12. Y. Sun, J. Phipps, D. S. Elson, H. Stoy, S. Tinling, J. Meier, B. Poirier, F. S. Chuang, D. G. Farwell, and L. Marcu, "Fluorescence lifetime imaging microscopy: in vivo application to diagnosis of oral carcinoma," *Opt. Lett.* **34**(13), 2081–2083 (2009).
13. T. J. Muldoon, D. Roblyer, M. D. Williams, V. M. T. Stepanek, R. Richards-Kortum, and A. M. Gillenwater, "Noninvasive imaging of oral neoplasia with a high-resolution fiber-optic microendoscope," *Head Neck* **34**(3), 305–312 (2012).
14. M.-T. Tsai, H.-C. Lee, C.-K. Lee, C.-H. Yu, H.-M. Chen, C.-P. Chiang, C.-C. Chang, Y.-M. Wang, and C. C. Yang, "Effective indicators for diagnosis of oral cancer using optical coherence tomography," *Opt. Express* **16**(20), 15847–15862 (2008).
15. B. Davoudi, A. Lindenmaier, B. A. Standish, G. Allo, K. Bizheva, and A. Vitkin, "Noninvasive in vivo structural and vascular imaging of human oral tissues with spectral domain optical coherence tomography," *Biomed. Opt. Express* **3**(5), 826–839 (2012).
16. D. Roblyer, C. Kurachi, V. Stepanek, M. D. Williams, A. K. El-Naggar, J. J. Lee, A. M. Gillenwater, and R. Richards-Kortum, "Objective detection and delineation of oral neoplasia using autofluorescence imaging," *Cancer Prev. Res. (Phila.)* **2**(5), 423–431 (2009).
17. M. W. Lingen, J. R. Kalmar, T. Karrison, and P. M. Speight, "Critical evaluation of diagnostic aids for the detection of oral cancer," *Oral Oncol.* **44**(1), 10–22 (2008).
18. C. F. Poh, C. E. MacAulay, D. M. Laronde, P. M. Williams, L. Zhang, and M. P. Rosin, "Squamous cell carcinoma and precursor lesions: diagnosis and screening in a technical era," *Periodontol.* **2000** **57**(1), 73–88 (2011).
19. I. Pavlova, M. Williams, A. El-Naggar, R. Richards-Kortum, and A. Gillenwater, "Understanding the biological basis of autofluorescence imaging for oral cancer detection: high-resolution fluorescence microscopy in viable tissue," *Clin. Cancer Res.* **14**(8), 2396–2404 (2008).
20. K. H. Awan, P. R. Morgan, and S. Warnakulasuriya, "Evaluation of an autofluorescence based imaging system (VELscope™) in the detection of oral potentially malignant disorders and benign keratoses," *Oral Oncol.* **47**(4), 274–277 (2011).
21. T. D. Wang and J. Van Dam, "Optical biopsy: A new frontier in endoscopic detection and diagnosis," *Clin. Gastroenterol. Hepatol.* **2**(9), 744–753 (2004).
22. J. G. Fujimoto, "Optical coherence tomography for ultrahigh resolution in vivo imaging," *Nat. Biotechnol.* **21**(11), 1361–1367 (2003).
23. A. M. Zysk, F. T. Nguyen, A. L. Oldenburg, D. L. Marks, and S. A. Boppart, "Optical coherence tomography: a review of clinical development from bench to bedside," *J. Biomed. Opt.* **12**(5), 051403 (2007).
24. P. Wilder-Smith, W. G. Jung, M. Brenner, K. Osann, H. Beydoun, D. Messadi, and Z. Chen, "In vivo optical coherence tomography for the diagnosis of oral malignancy," *Lasers Surg. Med.* **35**(4), 269–275 (2004).
25. A. Alex, M. Noti, E. D. T. Wojno, D. Artis, and C. Zhou, "Characterization of eosinophilic esophagitis murine models using optical coherence tomography," *Biomed. Opt. Express* **5**(2), 609–620 (2014).
26. W. J. Choi and R. K. Wang, "In vivo imaging of functional microvasculature within tissue beds of oral and nasal cavities by swept-source optical coherence tomography with a forward/side-viewing probe," *Biomed. Opt. Express* **5**(8), 2620–2634 (2014).
27. J. M. Ridgway, G. Ahuja, S. Guo, J. Su, U. Mahmood, Z. Chen, and B. Wong, "Imaging of the pediatric airway using optical coherence tomography," *Laryngoscope* **117**(12), 2206–2212 (2007).
28. I. Grulkowski, J. K. Nowak, K. Karnowski, P. Zebryk, M. Puszczewicz, J. Walkowiak, and M. Wojtkowski, "Quantitative assessment of oral mucosa and labial minor salivary glands in patients with Sjögren's syndrome using swept source OCT," *Biomed. Opt. Express* **5**(1), 259–274 (2014).
29. M.-T. Tsai, C. K. Lee, H. C. Lee, H. M. Chen, C.-P. Chiang, Y. M. Wang, and C. C. Yang, "Differentiating oral lesions in different carcinogenesis stages with optical coherence tomography," *J. Biomed. Opt.* **14**(4), 044028 (2009).

30. C. K. Lee, T. T. Chi, C. T. Wu, M. T. Tsai, C. P. Chiang, and C. C. Yang, "Diagnosis of oral precancer with optical coherence tomography," *Biomed. Opt. Express* **3**(7), 1632–1646 (2012).
31. P. Pande, S. Shrestha, J. Park, M. J. Serafino, I. Gimenez-Conti, J. Brandon, Y.-S. Cheng, B. E. Applegate, and J. A. Jo, "Automated classification of optical coherence tomography images for the diagnosis of oral malignancy in the hamster cheek pouch," *J. Biomed. Opt.* **19**(8), 086022 (2014).
32. O. K. Adegun, P. H. Tomlins, E. Hagi-Pavli, G. McKenzie, K. Piper, D. L. Bader, and F. Fortune, "Quantitative analysis of optical coherence tomography and histopathology images of normal and dysplastic oral mucosal tissues," *Lasers Med. Sci.* **27**(4), 795–804 (2012).
33. J. F. de Boer and T. E. Milner, "Review of polarization sensitive optical coherence tomography and Stokes vector determination," *J. Biomed. Opt.* **7**(3), 359–371 (2002).
34. J. F. de Boer, T. E. Milner, M. J. C. van Gemert, and J. S. Nelson, "Two-dimensional birefringence imaging in biological tissue by polarization-sensitive optical coherence tomography," *Opt. Lett.* **22**(12), 934–936 (1997).
35. K. H. Kim, M. C. Pierce, G. Maguluri, B. H. Park, S. J. Yoon, M. Lydon, R. Sheridan, and J. F. de Boer, "In vivo imaging of human burn injuries with polarization-sensitive optical coherence tomography," *J. Biomed. Opt.* **17**(6), 066012 (2012).
36. M. C. Pierce, R. L. Sheridan, B. Hyle Park, B. Cense, and J. F. de Boer, "Collagen denaturation can be quantified in burned human skin using polarization-sensitive optical coherence tomography," *Burns* **30**(6), 511–517 (2004).
37. M. Pircher, C. K. Hitznerberger, and U. Schmidt-Erfurth, "Polarization sensitive optical coherence tomography in the human eye," *Prog. Retin. Eye Res.* **30**(6), 431–451 (2011).
38. K. H. Kim, J. A. Burns, J. J. Bernstein, G. N. Maguluri, B. H. Park, and J. F. de Boer, "In vivo 3D human vocal fold imaging with polarization sensitive optical coherence tomography and a MEMS scanning catheter," *Opt. Express* **18**(14), 14644–14653 (2010).
39. W.-C. Kuo, N.-K. Chou, C. Chou, C.-M. Lai, H.-J. Huang, S.-S. Wang, and J.-J. Shyu, "Polarization-sensitive optical coherence tomography for imaging human atherosclerosis," *Appl. Opt.* **46**(13), 2520–2527 (2007).
40. S. K. Nadkarni, M. C. Pierce, B. H. Park, J. F. de Boer, P. Whittaker, B. E. Bouma, J. E. Bressner, E. Halpern, S. L. Houser, and G. J. Tearney, "Measurement of Collagen and Smooth Muscle Cell Content in Atherosclerotic Plaques Using Polarization-Sensitive Optical Coherence Tomography," *J. Am. Coll. Cardiol.* **49**(13), 1474–1481 (2007).
41. K. H. Kim, B. H. Park, Y. Tu, T. Hasan, B. Lee, J. Li, and J. F. de Boer, "Polarization-sensitive optical frequency domain imaging based on unpolarized light," *Opt. Express* **19**(2), 552–561 (2011).
42. M. A. Whitney, J. L. Crisp, L. T. Nguyen, B. Friedman, L. A. Gross, P. Steinbach, R. Y. Tsien, and Q. T. Nguyen, "Fluorescent peptides highlight peripheral nerves during surgery in mice," *Nat. Biotechnol.* **29**(4), 352–356 (2011).
43. D. C. Gray, E. M. Kim, V. E. Coterio, A. Bajaj, V. P. Staudinger, C. A. Hehir, and S. Yazdanfar, "Dual-mode laparoscopic fluorescence image-guided surgery using a single camera," *Biomed. Opt. Express* **3**(8), 1880–1890 (2012).
44. R. K. Orosco, R. Y. Tsien, and Q. T. Nguyen, "Fluorescence imaging in surgery," *IEEE Rev. Biomed. Eng.* **6**, 178–187 (2013).
45. M. C. Pierce, D. J. Javier, and R. Richards-Kortum, "Optical contrast agents and imaging systems for detection and diagnosis of cancer," *Int. J. Cancer* **123**(9), 1979–1990 (2008).
46. R. Weissleder, C. H. Tung, U. Mahmood, and A. Bogdanov, Jr., "In vivo imaging of tumors with protease-activated near-infrared fluorescent probes," *Nat. Biotechnol.* **17**(4), 375–378 (1999).
47. X. Gao, Y. Cui, R. M. Levenson, L. W. Chung, and S. Nie, "In vivo cancer targeting and imaging with semiconductor quantum dots," *Nat. Biotechnol.* **22**(8), 969–976 (2004).
48. S. Gioux, J. G. Coutard, M. Berger, H. Gâteau, V. Jossierand, M. Keramidias, C. Righini, J. L. Coll, and J. M. Dinten, "FluoSTIC: miniaturized fluorescence image-guided surgery system," *J. Biomed. Opt.* **17**(10), 106014 (2012).
49. Z. Luo, M. Loja, D. G. Farwell, Q. C. Luu, P. J. Donald, D. Amott, R. Gandour-Edwards, and N. Nitin, "High-Resolution Optical Molecular Imaging of Changes in Choline Metabolism in Oral Neoplasia," *Transl. Oncol.* **6**(1), 33–41 (2013).
50. H. Yoo, J. W. Kim, M. Shishkov, E. Namati, T. Morse, R. Shubochkin, J. R. McCarthy, V. Ntziachristos, B. E. Bouma, F. A. Jaffer, and G. J. Tearney, "Intra-arterial catheter for simultaneous microstructural and molecular imaging in vivo," *Nat. Med.* **17**(12), 1680–1684 (2011).
51. S. Liang, A. Saidi, J. Jing, G. Liu, J. Li, J. Zhang, C. Sun, J. Narula, and Z. Chen, "Intravascular atherosclerotic imaging with combined fluorescence and optical coherence tomography probe based on a double-clad fiber combiner," *J. Biomed. Opt.* **17**(7), 070501 (2012).
52. A. M. Winkler, P. F. S. Rice, J. Weichsel, J. M. Watson, M. V. Backer, J. M. Backer, and J. K. Barton, "In Vivo, Dual-Modality OCT/LIF Imaging Using a Novel VEGF Receptor-Targeted NIR Fluorescent Probe in the AOM-Treated Mouse Model," *Mol. Imaging Biol.* **13**(6), 1173–1182 (2011).
53. R. A. Wall and J. K. Barton, "Fluorescence-based surface magnifying chromoendoscopy and optical coherence tomography endoscope," *J. Biomed. Opt.* **17**(8), 086003 (2012).
54. N. Iftimia, A. K. Iyer, D. X. Hammer, N. Lue, M. Mujat, M. Pitman, R. D. Ferguson, and M. Amiji, "Fluorescence-guided optical coherence tomography imaging for colon cancer screening: a preliminary mouse study," *Biomed. Opt. Express* **3**(1), 178–191 (2012).

55. A. R. Tumlinson, L. P. Hariri, U. Utzinger, and J. K. Barton, "Miniature endoscope for simultaneous optical coherence tomography and laser-induced fluorescence measurement," *Appl. Opt.* **43**(1), 113–121 (2004).
56. Y. T. Pan, T. Q. Xie, C. W. Du, S. Bastacky, S. Meyers, and M. L. Zeidel, "Enhancing early bladder cancer detection with fluorescence-guided endoscopic optical coherence tomography," *Opt. Lett.* **28**(24), 2485–2487 (2003).
57. H. Pahlavaninezhad, A. M. D. Lee, S. Lam, C. MacAulay, and P. M. Lane, "Coregistered autofluorescence-optical coherence tomography imaging of human lung sections," *J. Biomed. Opt.* **19**(3), 036022 (2014).
58. L. M. Higgins and M. C. Pierce, "Design and characterization of a handheld multimodal imaging device for the assessment of oral epithelial lesions," *J. Biomed. Opt.* **19**(8), 086004 (2014).
59. J. M. Jabbour, S. Cheng, B. H. Malik, R. Cuenca, J. A. Jo, J. Wright, Y.-S. L. Cheng, and K. C. Maitland, "Fluorescence lifetime imaging and reflectance confocal microscopy for multiscale imaging of oral precancer," *J. Biomed. Opt.* **18**(4), 046012 (2013).
60. M. C. Pierce, R. A. Schwarz, V. S. Bhattar, S. Mondrik, M. D. Williams, J. J. Lee, R. Richards-Kortum, and A. M. Gillenwater, "Accuracy of In Vivo Multimodal Optical Imaging for Detection of Oral Neoplasia," *Cancer Prev. Res. (Phila.)* **5**(6), 801–809 (2012).
61. H. Fatakdawala, S. Poti, F. Zhou, Y. Sun, J. Bec, J. Liu, D. R. Yankelevich, S. P. Tinling, R. F. Gandour-Edwards, D. G. Farwell, and L. Marcu, "Multimodal in vivo imaging of oral cancer using fluorescence lifetime, photoacoustic and ultrasound techniques," *Biomed. Opt. Express* **4**(9), 1724–1741 (2013).
62. A. García-Hernández, R. Roldán-Marín, P. Iglesias-García, and J. Malvehy, "In vivo noninvasive imaging of healthy lower lip mucosa: a correlation study between high-definition optical coherence tomography, reflectance confocal microscopy, and histology," *Dermatol. Res. Pract.* **2013**, 205256 (2013).
63. M. Oheim, E. Beaurepaire, E. Chaigneau, J. Mertz, and S. Charpak, "Two-photon microscopy in brain tissue: parameters influencing the imaging depth," *J. Neurosci. Methods* **111**(1), 29–37 (2001).
64. B. Baumann, W. Choi, B. Potsaid, D. Huang, J. S. Duker, and J. G. Fujimoto, "Swept source/Fourier domain polarization sensitive optical coherence tomography with a passive polarization delay unit," *Opt. Express* **20**(9), 10229–10241 (2012).
65. Y. Lim, Y.-J. Hong, L. Duan, M. Yamanari, and Y. Yasuno, "Passive component based multifunctional Jones matrix swept source optical coherence tomography for Doppler and polarization imaging," *Opt. Lett.* **37**(11), 1958–1960 (2012).
66. B. H. Park, M. C. Pierce, B. Cense, and J. F. de Boer, "Jones matrix analysis for a polarization-sensitive optical coherence tomography system using fiber-optic components," *Opt. Lett.* **29**(21), 2512–2514 (2004).
67. B. H. Park, C. Saxer, S. M. Srinivas, J. S. Nelson, and J. F. de Boer, "In vivo burn depth determination by high-speed fiber-based polarization sensitive optical coherence tomography," *J. Biomed. Opt.* **6**(4), 474–479 (2001).
68. E. M. C. Hillman and S. A. Burgess, "Sub-millimeter resolution 3D optical imaging of living tissue using laminar optical tomography," *Laser Photon. Rev.* **3**(1-2), 159–179 (2009).

1. Introduction

Oral cavity lesions are becoming a significant health problem, which is further heightened due to personal habits [1]. Recent studies and statistical analysis showed that oral cancer is among top 10 most common diseases, and its incidence count and death rate are continuously increasing. Due to difficulty in the treatment of progressed cancer, early stage detection is crucial. Diagnostic methods of oral cancer included visual examination, biopsy, ultrasound backscatter microscopy (UBM) [2], cytology [3, 4], CT and MRI [5]. In addition, various optical imaging methods have been developed for the diagnosis and detection of oral cancer [6], with features of non- or minimal invasiveness, high resolution, high speed, molecular contrast, and relatively low cost. Available methods include spectroscopy [7, 8], autofluorescence imaging (AFI) and fluorescence lifetime imaging microscopy (FLIM) [9–12], fluorescent agent based imaging [13], optical coherence tomography (OCT) [14, 15].

Wide-field AFI is a highly sensitive imaging technique used for initial diagnosis of oral diseases [16, 17]. Using UV or blue light, wide-field AFI has potentials for detecting oral dysplasia, carcinoma *in situ*, and cancer based on the reduced fluorescence intensity [18]. However AFI has showed poor specificity because of confounding benign conditions including inflammation [19, 20]. AFI is also susceptible to thickness variation of the oral cavity layers such as the epithelium and lamina propria.

As a complementary imaging technique, OCT can provide information of under-surface tissue structure, microstructure, and vasculature non-invasively down to a few millimeter deep from the surface [21–23]. Feasibility of OCT as a diagnostic tool has been demonstrated in various pre-clinical animal [24, 25] and human [14, 26–30] oral cavity studies. Computational methods for automated OCT image analysis and classification [31],

quantitative assessment [28, 32] have been developed to aid diagnosis of oral cavity lesions. Polarization-sensitive OCT (PS-OCT) is an augmented OCT providing information of both structure and birefringence [33, 34]. PS-OCT is beneficial for birefringent tissues including the skin [35, 36], eye [37], vocal fold [38], coronary artery [39, 40], and oral cavity [41], because it provides additional contrast to distinguish lesions from normal tissues. PS-OCT of the oral cavity was demonstrated in a hamster cheek pouch cancer model [41]. The cancerous lesion was clearly distinguished from the surrounding normal tissue based on birefringence. Although PS-OCT has been applied to various pre-clinical and clinical studies, it has not been used much in the oral cavity.

Although OCT and PS-OCT have many advantages in visualizing microstructure, vasculature, and birefringence of tissue, they do not have molecular specificity. Fluorescence based imaging is a simple and effective way to achieve molecular specificities by using either intrinsic fluorescent molecules or extrinsic fluorescent agents. It can highlight various features within tissues such as the blood vessels, lymph nodes, and nerves which might be difficult to differentiate from surrounding in conventional white light examination [42–44]. For lesion detection, various fluorescent markers have been developed targeting specific receptors or enzymes that are abundant in lesions [44–49].

Multimodal approaches combining modalities of different contrast mechanisms may improve sensitivity and specificity by providing complementary information. Combinations of OCT and fluorescence imaging techniques have been developed and applied to various tissues such as the coronary artery [50, 51], colon [52–55], bladder [56], lung [57] and oral cavity [11, 58]. Other multimodal approaches for oral cavity detection include combinations of FLIM and reflectance confocal microscopy (RCM) [59], white light imaging and autofluorescence imaging [60], FLIM, UBM, and photoacoustic imaging (PAI) [61], and OCT and RCM [62].

In this paper, we developed a multimodal endoscopic imaging system by combining wide-field reflectance/fluorescence imaging and PS-OCT for human oral cavity *in vivo*. Wide-field reflectance/fluorescence imaging was to provide information of tissue surface based on reflectance and fluorescence, and PS-OCT was to provide information of under-surface structure and birefringence. A forward-viewing probe was designed to access the oral cavity through the mouth. Wide-field imaging was designed to have adjustable depth of focus (DOF) for being used as both image guiding and high-sensitivity imaging. Design and implementation of the multimodal imaging system was described. This multimodal method was characterized by imaging a tissue phantom and a mouse model, and applied to human oral cavity *in vivo* as a demonstration.

2. Materials and methods

2.1 Instrumentation

A schematic and a photograph of the multimodal imaging system are shown in Fig. 1. The multimodal system had an imaging probe of approximately 10 mm in diameter and 180 mm in length at its distal end for simultaneous wide-field reflectance/fluorescence imaging and PS-OCT through the mouth. As the wide-field reflectance/fluorescence imaging setup, a mercury lamp (Illuminator for IX71 microscope, Olympus) was used as the light source. A long-pass filter, which transmitted longer wavelength than 400 nm (FEL0400, Thorlabs), was installed in front of the lamp to block UV light. An additional excitation filter was added for fluorescence imaging. Light from the lamp was coupled into a liquid light guide (LLG0538-4, Thorlabs), and relayed to a bundle of plastic optical fibers (plastic optical fiber, PGR FB750, Toray industries). These fibers were glued together at one end for light coupling from the liquid guide, and were wrapped around the outer surface of the imaging probe at the other end for sample illumination. The liquid light guide was 5 mm in diameter and 1200 mm in length, and the plastic optical fiber bundle consisted of 49 fibers with 750 μm in diameter (0.5 NA).

Fluorescent light or reflected light from the sample was collected by the imaging probe. The imaging probe had three lenses (L1-L3) inside, and an optical window at its distal end for sealing. The optical window was slanted at 8° tilting angle with respect to normal to reduce back reflection. Fluorescent or reflected light from the sample passed through those lenses in the imaging probe, a dichroic mirror (DM, 1025dcspxr, Chroma), an emission filter, and finally focused by a lens (L4) on a charge coupled device (CCD) camera (12-bit QIClick digital camera, QImaging). Those lenses (L1-L3) in the imaging probe were 9 mm in diameter with 40 mm in focal length, and the lens (L4) was 25 mm in diameter with 40 mm in focal length. All of those lenses were positioned in 4-f configuration to relay light from the sample to the camera with 1:1.8 magnification. The dichroic mirror transmitted visible light and reflected OCT light of 1300 nm in wavelength. The emission filter between DM and L4 was designed to be removable for easy switching between reflectance and fluorescence modes. A diaphragm (SM1D12SZ, Thorlab) was placed to control detection NA for DOF adjustment [63].

A custom PS-OCT system based on passive delay unit (PDU) [64, 65] was used in this study. In short, the system used a wavelength swept-source (SSOCT-1310, AXSUN Technologies), which had its center wavelength of 1310 nm, bandwidth of 107 nm, sweeping speed of 50 KHz. This PS-OCT method took advantages of a long coherence length of the source which was 6 mm in the air. PDU consisting of a polarizer, a polarizing beam splitter, and two delay lines was used to generate two orthogonal polarization states with optical path-length difference of 2.25 mm in the air. The two polarization states illuminated the sample, their reflection was detected simultaneously in the single image. Light from the source was split with a 95:5 ratio: 95% of light went to the interferometry setup for OCT, and 5% went to a fiber Bragg grating (FBG) to generate an external trigger signal for data acquisition. In the interferometer, light was split into the reference and sample arms with a 20:80 ratio respectively by a fiber coupler. Light in the sample arm first passed through a PDU, and then was delivered by an optical fiber, collimated to 1.8 mm in diameter with a fiber collimator (HPUCO-13A-1300/1550-S-11AS, OZ optics). The illumination beam was reflected on a mirror and galvanometric x-y scanner (GVS002, Thorlabs), relayed by the pair of a scan lens (SL) and a tube lens (TL), reflected on the dichroic mirror, relayed by the lenses in the tube, and then focused on to the sample with effective numerical aperture (NA) of 0.0225. The focal plane was approximately 23 mm away from the imaging probe. Scattered light from the sample was collected by L1, traced back in the same path as the illumination beam to the fiber collimator, and sent to the detection arm of OCT setup. Reflected light from the sample was combined with light from the reference arms at the detection arm, and interference signals were collected by two balanced photodetectors (PDB410C, Thorlabs) in the polarization diverse detection setup. Data was post-processed to get both intensity and PS images. Dispersion difference between the reference and sample arms was compensated numerically by using pre-calibration data of a mirror sample. The signal-to-noise ratio of our system is 103 dB. PS-OCT images were taken with the lateral scan over 5 mm x 5 mm which corresponding to 500 pixels x 500 pixels, imaging time was 6 seconds for each volume scan. Simultaneous sample probing with two polarization states enabled determination of the depth-resolved Jones matrices of the sample. Polarization properties of the sample were obtained by analyzing the sample Jones matrices through eigenvector decomposition [41, 66].

The multimodal imaging probe was built on a breadboard, which was mounted on an articulated arm (ET arm-B3, Aceluxe) for flexible positioning as shown in Fig. 1(b). Both the position and angle of the probe could be easily adjusted during imaging. The entire multimodal system was built on a portable cart providing movement which can be essential for uses in clinical trials.

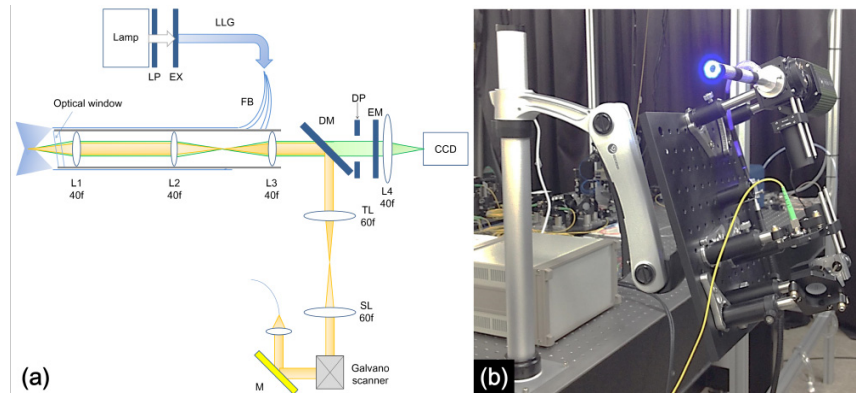


Fig. 1. (a) Schematic of the multimodal imaging probe. DM: dichroic mirror, L1-L4: lenses, M: mirror, SL: scan lens, TL: tube lens, LP: long pass filter, EX: excitation filter, EM: emission filter, DP: diaphragm, LLG: liquid light guide, FB: optical fiber bundle. Excitation and emission beams were depicted in blue and green respectively, and OCT beam was depicted in orange. (b) Photograph of the multimodal imaging probe mounted on an articulated arm.

2.2 Sample preparation and experiment procedure

A tissue phantom made of yellow-green fluorescent microspheres (Fluosphere 505/515, 10 μm in diameter, Invitrogen) embedded in 2% agarose gel was used to characterize the multimodal imaging system. For the characterization with an animal model, a Balb/C mouse was used. The mouse was obtained from the Jackson Laboratory, and bred at the animal facility of POSTECH Biotech Center (PBC). Fluorescein isothiocyanate (FITC)-dextran conjugates (500 μg in 100 μl PBS, Sigma) in 150 μl was injected at the tail vein for the visualization of vasculature. After 5 min of injection, the mouse was anesthetized with isoflurane gas, and the ear was attached on the slide glass to be flat by using double-sided tape for imaging. Wide-field reflectance/fluorescence imaging were performed by using a combination of excitation and emission filters. Two bandpass filters (ET455/50 and ET525/50, Chroma) were used as the excitation and emission filters respectively for fluorescence imaging of fluorescent microsphere and mouse ear samples. A bandpass filter having 50 nm bandwidth around 525 nm (ET525/50, Chroma) was used to do reflectance imaging of human oral cavity tissues. Wide-field reflectance/fluorescence and OCT images were displayed on computer screens in real-time and acquired simultaneously.

2.3. Characterization

Performance of the multimodal imaging system was characterized by imaging the fluorescent microsphere sample and the results are shown in Fig. 2. A wide-field reflectance image (Fig. 2(a), a wide-field fluorescence image (2(b)), and a zoomed fluorescence image (2(c)) in the x-y plane, and an OCT image (2(d)) in the x-z plane are shown respectively. The power at the sample and exposure time for wide-field reflectance and fluorescence imaging was 10.6 mW / 30 ms and 10.2 mW / 4 s respectively. Reflectance image showed microsphere distribution with high background which might be due to reflection from the sample surface. On the other hand, fluorescence image showed individual microspheres clearly with much less background. In zoomed fluorescence image of the boxed region in Fig. 2(b), individual microspheres were resolved indicating the image resolution comparable with the microsphere size which was 10 μm in diameter. To characterize the effective field of view (FOV), full width at half maximum intensity (FWHM) of the illumination field was quantified by using a reflection target and it was approximately 5.5 mm and 6.1 mm in the x and y axes respectively. The spatial resolution of wide-field reflectance and fluorescence was calculated based on the edge-spread function and point spread function using a sharp edge specimen and

6 μm fluorescent microspheres. The spatial resolution of wide-field reflectance and fluorescence were approximately 13 μm and 15.7 μm , respectively. Although theoretical lateral resolution based on maximum NA of 0.075 and wavelength of 525 nm was calculated to be 3.75 μm , and the minimal resolvable size by the CCD camera was 12.9 μm in the sample in consideration of the CCD pixel size of 6.45 μm and magnification of 1x. Therefore, the theoretical resolution was limited by pixelation of the CCD camera in the current configuration.

For OCT imaging 6.8 mW at the focal plane was used. OCT cross-sectional image visualized microsphere distribution in the x-z plane. OCT intensity image displayed the logarithmic intensity in a gray scale where white and black indicated the lowest and highest intensities respectively. Microspheres appeared in both fluorescence and OCT images since they emitted fluorescence light and scattered illumination light. 3D volumetric OCT images were obtained by acquiring multiple cross-sectional images in the x-z plane with stepwise increments in the y direction. Each 2D OCT images had 500 x 500 pixels in the x-y plane, composing a 3D volumetric OCT image of 5.5 mm x 5.5 mm x 3.3 mm in size. FOV was approximately 5.5 mm in diameter, and depth of focus (DOF) was 2.1 mm in the tissue. Acquisition time was approximately 5 seconds per 3D volume. For PS-OCT imaging the spatial resolution was measured by imaging the microspheres and a mirror. Full width half maximum (FWHM) intensity was calculated as 15 μm and 12.5 μm in the lateral and axial directions in the air, respectively.

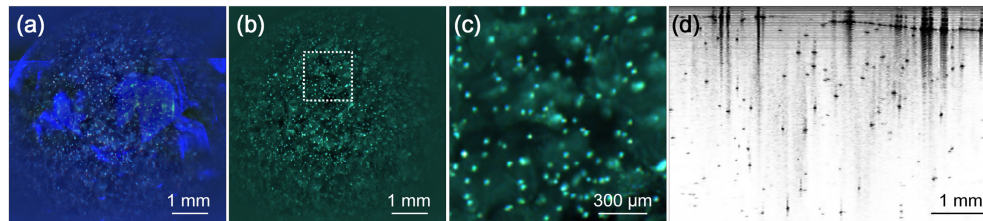


Fig. 2. Multimodal images of fluorescent microspheres: (a) wide-field reflectance image, b) wide-field fluorescence image, (c) zoomed fluorescence image of boxed region in Fig. 2(b) d) cross-sectional OCT image.

DOF of wide-field imaging was measured as a function of detection NA and results are shown in Fig. 3. DOF was measured by using a DOF target (#54-440, Edmund Optics) which had a black-white pattern with 15 lines/mm on its surface slanted by 45° from the horizontal surface. Detection NA was varied from 0.075 to 0.0125 by controlling the diaphragm aperture. Images of the DOF target with different NAs of 0.075, 0.0625, and 0.0125, and measured DOF as a function of detection NA are shown in Fig. 3(a)–3(c) and 3(d) respectively. DOF target images showed increase of DOF with detection NA decrease. DOF was measured by counting number of visible patterns in DOF images. Measured DOF was compared with theoretical DOF based on Rayleigh range in Fig. 3(d). Although measured DOF followed the trend of theoretical DOF, there was some offset between them. Adjustable DOF range in the current configuration was from 1 mm to 10 mm.

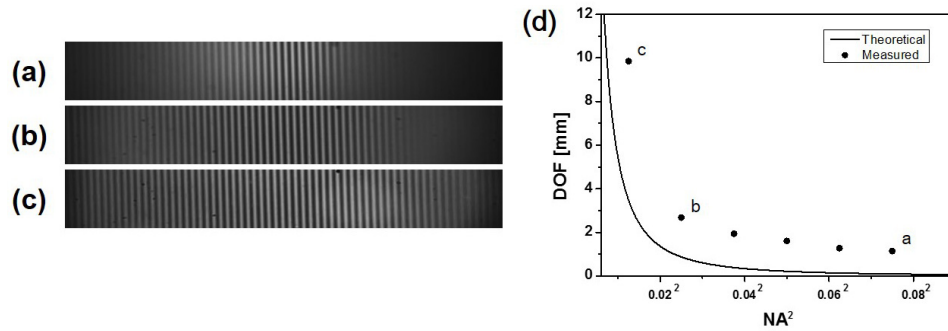


Fig. 3. Measurement of DOF of the wide-field imaging with detection NA. (a – c) DOF change image at different NA setting, 0.075, 0.0625 and 0.0125, respectively (d) relation between measured DOF and NA^2 .

3. Results

3.1 Mouse ear *in vivo*

The multimodal imaging probe was applied to the mouse ear *in vivo*, and results are shown in Fig. 4. Wide-field reflectance/fluorescence images and an OCT cross-sectional image are shown in Fig. 4(a), 4(b), 4(c), and 4(d), respectively. Reflectance image, acquired with white light illumination, showed relatively large blood vessels in red color due to strong light absorption by hemoglobin. Fluorescence image showed the blood vessels more clearly based on FITC-dextran fluorescence. Boxed region in Fig. 4(b) was magnified and shown in Fig. 4(c). The magnified fluorescence image clearly visualized small blood vessels branching out from big vessels close to the surface. Fluorescence image using FITC-dextran was to show the feasibility of *in vivo* tissue imaging. OCT cross-sectional image visualized microstructures of the entire ear thickness which was approximately 300 μm . The epidermis and dermis on both sides of the skin and the cartilage in the middle, were shown.

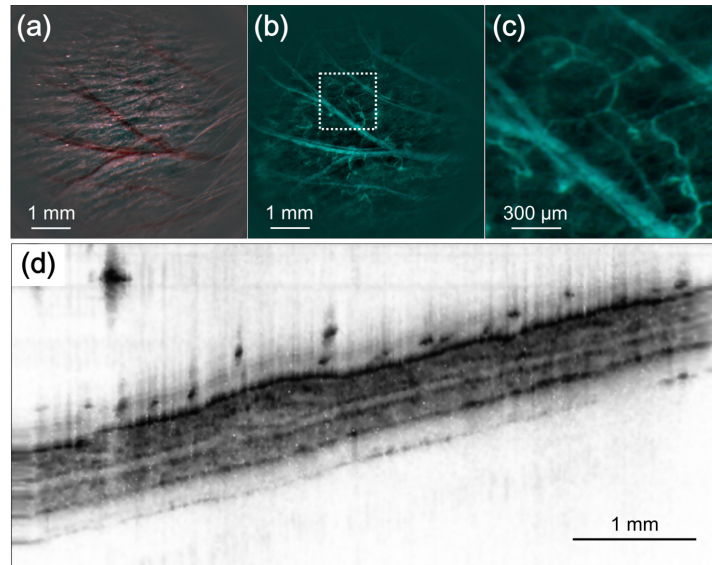


Fig. 4. Images of mouse ear taken by the multimodal imaging probe. (a) Reflectance image, (b) fluorescence image, (c) magnified fluorescence image of the boxed region in (b), (d) OCT cross-sectional image ([Media 1](#)).

3.2 Human oral cavity in vivo

The multimodal imaging system was applied to two different regions of oral cavity of a human volunteer. Images of the tongue and buccal mucosa are shown in Fig. 5 and 6, respectively. A wide-field reflectance image, en face OCT image and PS-OCT images of the tongue are shown in Fig. 5(a), 5(b) and 5(c), 5(d), respectively. Wide-field reflectance and en face OCT image showed small, rounded nipples, called lingual papillae distributed on the surface of dorsum of tongue in Fig. 5(a) and 5(b). The cross-sectional OCT intensity image of the white dashed line in Fig. 5(b) showed rough tongue surface due to the distribution of papillae (red arrow in Fig. 5(c)), and relative homogeneous under-surface structures. PS image of the tongue showed changes in the gray scale from black to white with depth. PS image displayed the accumulated phase retardation with depth from the tissue surface in a gray scale where black and white colors corresponded to 0° and 180° phase retardations respectively. Further accumulation of phase retardation wraps back around to a black color [67]. Changes in the gray scale with depth in the PS image of the tongue indicated changes in the phase retardation, and therefore the presence of birefringence. Birefringence was characterized by estimating the slope of the accumulated phase retardation with depth in the PS image.

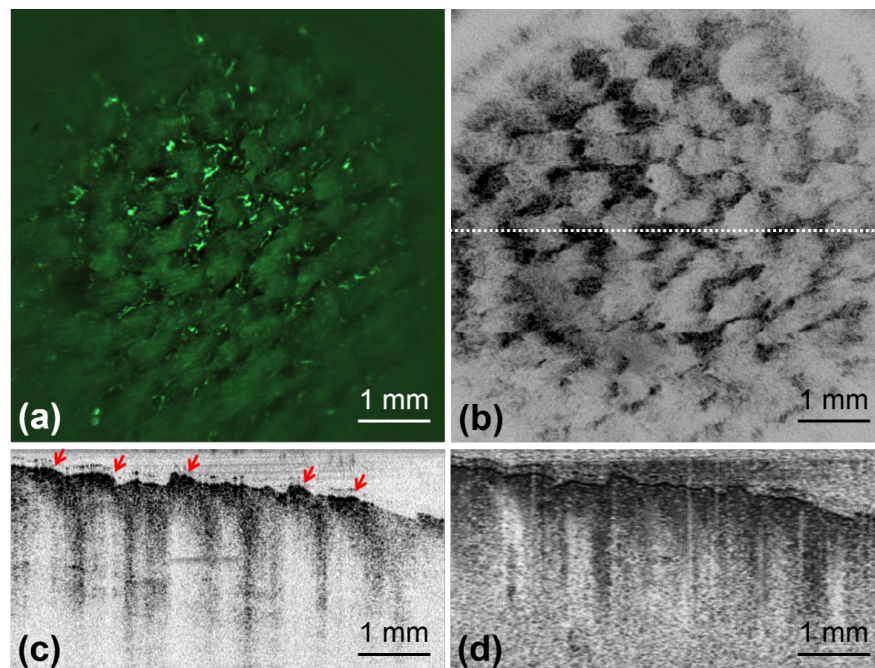


Fig. 5. Multimodal images of human tongue. (a) Wide-field reflectance image, (b) en face OCT image, (c, d) Cross-sectional OCT intensity and PS images respectively. Red arrows in (c) indicate lingual papillae spread across the surface of tongue. ([Media 2](#)).

A wide-field reflectance image and PS-OCT images of human buccal mucosa are shown in Fig. 6(a) and 6(b), 6(c), respectively. Wide-field reflectance image showed vasculature in the superficial mucosa in negative contrast due to light absorption as shown in Fig. 6(a). OCT intensity image showed layered structures of the mucosa such as the oral epithelium (EP), lamina propria (LP), submucosa (SM). EP consisting of the epithelial cells had lower intensity compared to LP consisting of collagen, and SM was also distinguished based on intensity difference. PS image showed color changes with depth from the surface. EP remained black indicating no birefringence, and both LP and SM showed color changes from black to white and then to black indicating birefringence. LP and SM are known to be

birefringent due to collagen composition and highly ordered arrangement of muscle, respectively.

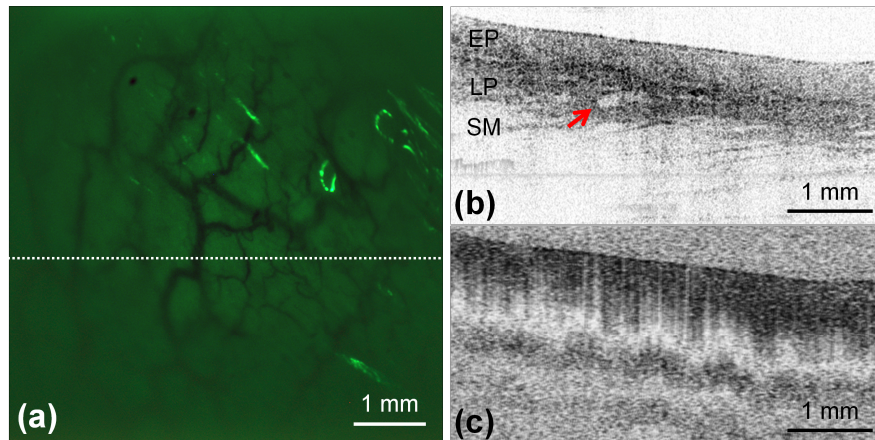


Fig. 6. Multimodal image of human buccal mucosa. (a) wide-field reflectance image, (b, c) Cross-sectional OCT intensity and PS image. EP: epithelium, LP: lamina propria, SM: submucosa, M: muscle (red arrow indicates blood vessels) ([Media 3](#)).

4. Discussions

The multimodal imaging system based on wide-field reflectance/fluorescence imaging and PS-OCT was developed, and applied to human oral cavity *in vivo* using the forward-viewing probe. This multimodal method provided information of morphology, vasculature of superficial region of the oral cavity and information of layered structure, birefringence down to a few millimeters from the surface. Wide-field imaging helped to find the region of interest of the sample based on light reflection. Vasculatures are detected with negative contrast due to optical scattering and absorption in blood. With PS-OCT, not only 3D structures of composing layers but also birefringence structures of the tissue could be imaged. Intensity OCT image revealed constituting layers of buccal mucosa, such as epithelium, lamina propria, and submucosa. The muscle layer inside tissue have strong birefringent property, which is presented in black and white banding pattern in PS image.

Implementation of the adjustable diaphragm, providing DOF from 2 mm to 10 mm, can be advantageous in practical situations. With high DOF, image guiding or screening can be performed, whereas low DOF allows detailed imaging with high-resolution/high-sensitivity. Measured DOFs as a function of detection NAs showed relatively good tendency with theoretical DOF. However there was a slight offset in practice, since resolvable distance between each line of DOF target was over measured. Also, the imperfect adjustment of diaphragm might have affected the offset.

Current multimodal imaging system still has a number of rooms to improve. The current configuration of wide-field reflectance/fluorescence was not able to do autofluorescence imaging (AFI), which has been used for initial oral cavity screening in the clinic, simply because the CCD camera used was not sensitive enough to detect autofluorescence. The current CCD camera was a color camera which was good for wide-field reflectance imaging and also feasible for fluorescence imaging with exogenous fluorescent probes. A system upgrade in the camera would be required for the simultaneous AFI and PS-OCT. In order to secure large FOV of approximately 6 mm in diameter, the current imaging probe has an approximate diameter of 10 mm with the use of 9 mm diameter lenses. The size of the imaging probe can be reduced for applications that require smaller FOV. Illumination for wide-field reflectance/fluorescence imaging was not uniform throughout the FOV: stronger in the middle and dimmer in the periphery (noticeable in Fig. 5(a) and Fig. 6(a)). Redesigning

the end of the illumination fiber could improve mentioned limitation. There was some surface reflection in human oral cavity imaging, the use of cross-polarizers in the illumination and detection paths could minimize such surface reflectance. In the present configuration, filters were manual changed to switch between the wide-field reflectance and fluorescence imaging. Motorized filter wheels will be implemented for automatic switching between the two modes. In the acquired 3D PS-OCT images an artifact, possibly risen from either contamination of optics or the surface reflection of the lens, appeared in the image. In the future, replacement of the contaminated lens series could reduce the artifacts shown in PS-OCT images. Furthermore, current multimodal imaging probe can be improved by incorporating 3D fluorescence imaging techniques such as laminar optical tomography (LOT) [68]. Other OCT techniques such as angiographic OCT can be added to provide more contrast in current OCT to identify abnormal lesions.

Acknowledgments

We would like to thank Seoyeon Bok at POSTECH for tail vein injection of FITC-dextran conjugate in mice tail. This work is supported in part by the Engineering Research Center grant (No. 2011-0030075) and the Bio and Medical Technology Development Program (No. 2011-0019633) of the National Research Foundation (NRF) funded by the Korean government (MEST), and National R&D Program for Cancer Control (No. 1320220) by National Cancer Center Korea.